

NRC Publications Archive Archives des publications du CNRC

Investigation of the feedstock deposition behavior in a cold sprayed 316L/Fe composite coating

Chu, Xin; Chakrabarty, Rohan; Che, Hanqing; Shang, Lihong; Vo, Phuong;
Song, Jun; Yue, Stephen

This publication could be one of several versions: author's original, accepted manuscript or the publisher's version. /
La version de cette publication peut être l'une des suivantes : la version prépublication de l'auteur, la version
acceptée du manuscrit ou la version de l'éditeur.

For the publisher's version, please access the DOI link below. / Pour consulter la version de l'éditeur, utilisez le lien
DOI ci-dessous.

Publisher's version / Version de l'éditeur:

<https://doi.org/10.1016/j.surfcoat.2017.12.063>

Surface & Coatings Technology, 337, pp. 53-62, 2017-12-29

NRC Publications Archive Record / Notice des Archives des publications du CNRC :

<https://nrc-publications.canada.ca/eng/view/object/?id=3ca741d4-b36a-4973-a6dc-9de1e6f8077d>

<https://publications-cnrc.canada.ca/fra/voir/objet/?id=3ca741d4-b36a-4973-a6dc-9de1e6f8077d>

Access and use of this website and the material on it are subject to the Terms and Conditions set forth at

<https://nrc-publications.canada.ca/eng/copyright>

READ THESE TERMS AND CONDITIONS CAREFULLY BEFORE USING THIS WEBSITE.

L'accès à ce site Web et l'utilisation de son contenu sont assujettis aux conditions présentées dans le site

<https://publications-cnrc.canada.ca/fra/droits>

LISEZ CES CONDITIONS ATTENTIVEMENT AVANT D'UTILISER CE SITE WEB.

Questions? Contact the NRC Publications Archive team at

PublicationsArchive-ArchivesPublications@nrc-cnrc.gc.ca. If you wish to email the authors directly, please see the
first page of the publication for their contact information.

Vous avez des questions? Nous pouvons vous aider. Pour communiquer directement avec un auteur, consultez la
première page de la revue dans laquelle son article a été publié afin de trouver ses coordonnées. Si vous n'arrivez
pas à les repérer, communiquez avec nous à PublicationsArchive-ArchivesPublications@nrc-cnrc.gc.ca.

Investigation of the Feedstock Deposition Behavior in a Cold Sprayed 316L/Fe Composite Coating

Xin Chu ^{a*}, Rohan Chakrabarty ^a, Hanqing Che ^a, Lihong Shang ^a, Phuong Vo ^b, Jun Song ^a, and
Stephen Yue ^a

a. Department of Mining and Materials Engineering, McGill University, Montreal, Quebec H3A 0C5, Canada

b. National Research Council Canada, Boucherville, Quebec J4B 6Y4, Canada

*Corresponding author: Xin Chu

Email: xin.chu@mail.mcgill.ca

Tel: +1 438.388.0632

Present address: 2370-3610 University, Montreal, Quebec, H3A 0C5, Canada

Abstract:

Mixing powders in cold spray is a straightforward method to produce composite coatings, but a direct interpretation of the mixed powder deposition behavior from coating microstructure is often difficult. In this study, to investigate the feedstock deposition behavior in a cold sprayed 316L-10 wt.% Fe (10Fe) metal-metal composite coating, splats deposited onto the as-polished 316L and Fe coatings with four types of impact scenarios were studied: (i) 316L on 316L, (ii) 316L on Fe, (iii) Fe on 316L, and (iv) Fe on Fe. The splat flattening ratio and coating crater depth/diameter were measured using a light optical microscope (LOM) and an optical profilometer to evaluate the degrees of particle and coating deformation. Finite element (FE) simulations were performed to obtain the splat rebound behavior during impact. A modified ball bond shear test was performed to determine the adhesion strength/energy of the cold spray splats. Results reveal distinct interparticle bonding features in the 10Fe coating, especially at the mixed 316L/Fe interfaces where a preferential location of inter-lamellar cracks can be seen. Similar bonding features were also observed in the deposited splats, indicating the splat on coating tests to be indicative of the coating build-up process. Finally, the feedstock deposition behavior in the 10Fe coating was explained through splat characterizations and FE simulations from hardness, surface oxide layer and particle morphology.

Keywords: Cold spray; Mixed powder; Deposition behavior; Splat test; Deformation; Adhesion

1. Introduction

Cold spray can be an effective alternative to fabricate metal matrix composites (MMC) due to its low process temperature which minimizes the oxidation and chemical degradation of the feedstock. Some typical examples extensively studied by researchers are metal-ceramic composites, e.g. WC-based [1-6] and Al₂O₃-based [7-11]. Cold spray utilizes the plastic deformability of the metal thus the brittle ceramic can be deposited. Compared with metal-ceramic composites, however, relatively few studies of cold spraying metal-metal composites are reported, in particular, concerning the feedstock deposition behavior [12-14].

Among the various strategies to obtain composite coatings in cold spray, e.g. coating or mechanically milling the powders, mixing powders (pre-blending and dual feeding) is a straightforward approach [15, 16]. This method enables free interactions between the mixed components during flight and upon impact, which can lead to an improved cold sprayability of the component powder, e.g. reduced porosity and increased deposition efficiency (DE) [13, 17-21]. Whereas unlike metal-ceramic mixtures, where the impinging ceramic powders only contribute to tamping and roughening of the surface layers [20], almost all metal powders can exhibit certain degrees of cold sprayabilities and this generates uncertainties of the feedstock deposition behavior at mixed metal-metal interfaces. Thus, it is often difficult to prescribe the suitable process parameters for a specific metal-metal mixture in cold spray.

The coating formation process in cold spray incorporates, but is not limited to, the individual deposition behavior of a single particle [22]. Other factors such as characteristics of the previously deposited layers and the successive peening/erosion of the subsequent particles can all affect the individual particle deposition [22]. Individual particle impact tests (or splat tests) can be considered as a monolayer coating deposition and is often used to study the coating deposition onset [23]. Due to the low investment in gas and feedstock material, the splat test is a

suitable trial-and-error approach to explore the cold spray feasibility or to identify the optimal process parameters of specific particle/substrate combinations. As effects of successive tamping and surface roughness are avoided by performing splat tests, the individual behavior of a feedstock during deposition can be clearly observed, e.g. particle deformation, rebound, and jetting. Moreover, the splat behavior can often be indicative of several coating cold sprayability metrics (e.g. adhesion [24] and DE [25]) in the case of the similar particle and substrate material.

Splat tests are usually generated by low feed rate spraying of single particles onto an as-polished substrate. In a previous work [26], single component 316L, Fe, and composite 316L/Fe coatings were cold sprayed deposited and splat tests were performed onto the as-polished coatings. It was observed that the partial DE of the feedstock components in composite coatings can be indicated by the respective splat bond ratio in splat tests. This motivates us to study the single splats in order to investigate the feedstock deposition behavior in the composite coating, since a direct interpretation of it from coating microstructure is difficult. In this study, the feedstock deposition behavior in a 10Fe composite coating was mainly investigated. The interparticle bonding features in the cold sprayed coatings and deposited splats were discussed and compared. Experimental characterizations and finite element (FE) simulations of the splats were performed to explain the feedstock deposition behavior in the 10Fe coating.

2. Materials and Methods

2.1 Experiments

Commercially available 316L stainless steel powder (Sandvik Osprey, Neath-Port Talbot, UK) and commercial purity Fe powder (Quebec Metal Powders, Sorel-Tracy, Canada) were used as the feedstock. SEM images of the feedstock are shown in Fig. 1 and characteristics of the feedstock are presented in Table 1. The average particle size was determined using a Horiba LA-920 laser diffraction analyzer (Horiba, Tokyo, Japan). The average Vickers hardness of the feedstock was measured using a Clark CM-100AT Microhardness Tester (Sun-Tec, Novi, USA) for a penetration time of 15 s under 10 g load.

Spraying was performed at the McGill-NRC cold spray facility, located at the National Research Council Canada, Boucherville, using a Plasma Giken PCS-800 cold spray system (Plasma Giken, Yorii-machi, Japan) with a PNFC2-010-30S carbide nozzle. Nitrogen was used as the propellant gas and the process parameters were set at a gas preheating temperature of 700 °C, a gas pressure of 4 MPa, and a stand-off distance of 80 mm. Coatings with nominal compositions of 100 wt.% 316L (316L), 90 wt.% 316L-10 wt.% Fe (10Fe), and 100 wt.% Fe (Fe) were deposited (a dual feeder was used to deposit the composite coating) on mild steel substrates. The splat tests were performed by spraying 316L or Fe powder onto the single component 316L and Fe coatings. The coatings used as substrates for splat tests all have a thickness of about 1 mm in order to eliminate the effect of the mild steel substrate, and they were polished beforehand to a mirror surface. The process details regarding coating deposition and splat tests are shown in Table 2.

After coating deposition, DE was measured as the mass gain of the substrate divided by the total mass of spray material fed over the substrate. The coating cross-sections were

characterized by a Hitachi SU3500 SEM (Hitachi, Tokyo, Japan). After splat tests, micrographs of coating surfaces and splats were observed by SEM. The splat deposition behavior was evaluated using bond ratio (BR). As previously discussed in [26], BR was determined as the average value of the fraction of the number of bonded particles (splats) to the total incident particles (splats+craters). The splats and craters from about 3-5 SEM images of the center of spray line with a field of $640 \times 480 \mu\text{m}$ were counted for each impact scenario. The total numbers of splats+craters in a single image are about 240-300 for 316L impact and about 130-180 for Fe impact. The degree of splat deformation was evaluated by the flattening ratio, which was calculated as the width over the height of a cross-sectioned splat. The degree of coating deformation was evaluated by a fraction of the depth of the crater over its diameter using a Zygo NewView 8000 optical profilometer (Zygo Corp., Middlefield, USA). Over 30 splats and craters were measured to calculate the respective flattening ratio and coating crater depth/diameter, and the average values were reported.

Splat adhesion tests were performed in reference to [24, 27] using a Micro-Combi Scratch Tester (CSM Instruments Inc., Needham, USA) equipped with a wedge shaped stylus. Prior to testing, the average diameter of splat was measured by the integrated LOM to calculate the splat area (A). During tests, a constant normal force, F_N , of 100 or 300 mN was applied onto the stylus, which is $100 \mu\text{m}$ in the tip width. The substrate was moving at a $150 \mu\text{m}/\text{min}$ rate below the stylus to create a shearing behavior. When the stylus encountered the splat edge, the tangential force (F_T) gradually increased to a peak and then dropped sharply at splat failure (see Fig. 2). For each sample, between four to eight splats of 40 to $50 \mu\text{m}$ in diameter were shear tested. After testing, the adhesion strength was calculated using the peak tangential force ($F_T(\text{Peak})$) subtracting the baseline tangential force ($F_T(\text{Baseline})$). The adhesion energy (an energy required to debond the splat) was calculated by integrating the area under tangential force curve.

This was normalized to the projected area of the splat (A). Similarly, the baseline friction force area was subtracted from the peak.

$$\text{Adhesion strength} = \frac{F_T(\text{Peak}) - F_T(\text{Baseline})}{A} \quad (1)$$

$$\text{Adhesion energy} = \frac{\int_{\text{Contact}}^{\text{Failure}} (F_T(x) - F_T(\text{Baseline})) dx}{\text{Projected Splat Area}} \quad (2)$$

2.2 FE simulations

A 2D Lagrangian axisymmetric model was used to obtain the splat rebound behavior during impact using the FE analysis software ABAQUS/Explicit (version 6.11-1) [28]. The size of the feedstock was set to be the same as the one listed in Table 1. The velocities of the feedstocks were set at 585 m/s for 316L and 600 m/s for Fe, which were measured by a Coldspraymeter particle diagnostic system (Tecnar Automation, St. Bruno, CA) [20]. The dimensions of the substrate were set to be 10 times the particle radius to eliminate influence from boundary conditions. A 4-node bilinear plane strain quadrilateral mesh (CPE4R) was used for the simulation. A convergence study was carried out and a meshing resolution of 1/50 D_p (diameter of the particle) was considered for the particle and the substrate. This meshing resolution has been used in earlier studies [29, 30]. Distortion and hourglass controls were kept at default settings. Symmetry boundary conditions were imposed on the sides of the particle and substrate, while the bottom of the substrate was fixed. The elastic response of the material was assumed isotropic while the plastic response of the material was described by the Johnson-Cook plasticity model [31].

$$\sigma = [A + B\varepsilon^n][1 + C \ln \varepsilon^*][1 - T^{*m}] \quad (3)$$

$$T^{*m} = (T - T_{ref}) / (T_m - T_{ref}) \quad (4)$$

where σ is the flow stress, ε is the equivalent plastic strain (PEEQ) defined as $\varepsilon = \int_0^t \sqrt{\frac{2}{3} \dot{\varepsilon}^{pl} : \dot{\varepsilon}^{pl}} dt$, with $\dot{\varepsilon}^{pl}$ being the plastic strain rate, $\dot{\varepsilon}^*$ is the equivalent plastic strain rate normalized by a reference strain rate, T_{ref} is the reference temperature and T_m is the melting temperature [25, 29, 30, 32]. In our simulations the deformation process is considered to be adiabatic due to the high rate of deformation, as previously explained by Assadi et al. [29]. The initial temperature of both the particle and substrate is kept at room temperatures (298K). The material properties and parameters for the Johnson-Cook model are tabulated in Table 3 [33, 34].

To obtain the splat rebound behavior, the splat recoil coefficient e_r was determined. Recoil coefficient e_r defines the proportion of the particle kinetic energy to be rebounded upon impact due to elastic recovery and is given as [35]:

$$e_r = 11.47 \left(\frac{\bar{\sigma}_Y}{E^*} \right)^{\frac{5}{4}} \rho_p^{-\frac{1}{4}} v_p^{-\frac{1}{2}} \quad (5)$$

where ρ_p , m_p , and v_p are respectively, the density, particle weight, and velocity of impacted particles, $\bar{\sigma}_Y$ is the particle effective yield stress during impact determined from FE simulations, and E^* is an elastic modulus that is experienced during particle impact.

3. Results

3.1 Characterization of coatings

The DE and BSE images of the single component 316L and Fe coatings are shown in Fig. 3. The 316L coating (Fig. 3 (a)) reveals small amounts of porosity (black regions) while the Fe (Fig. 3 (b)) has a dense structure. In cold sprayed coatings, the native oxide scales of the feedstock powder will be included and are presented between particles delineating as the interparticle boundaries (dark lines). By observing the interparticle boundaries of the 316L and Fe, a significant difference is revealed. The Fe/Fe particle interfaces in Fig. 3 (b) are seen to be wider and more clearly delineated compared to the 316L/316L interfaces in Fig. 3 (a), indicating a poorer interfacial bonding of the Fe coating than 316L. This feature can be attributed to the high oxidation susceptibility of the Fe particles, and also appears to be consistent with a slightly inferior DE of the single component Fe to that of 316L (50% vs 55%). EDS scans were then performed on the 316L and Fe coatings at interparticle regions and also inner particle regions as a reference. As shown in Figs. 3 (c) and (d), the EDS spectra indicate the presence of oxygen at interparticle regions and the complete absence at inner particle regions. Thus, it is suggested that the dark lines in BSE images represent the oxide scale on the powder surface, and the Fe has a thicker oxide scale compared with 316L.

The DE and BSE image of the 10Fe composite coating are shown in Fig. 4. The impact direction is indicated by the white arrow, and the dark regions are Fe, the light regions are 316L, and the black spots are pores. For the 10Fe composite coating, the mixed 316L/Fe interfaces are generated. Firstly, comparing the non-mixed 316L/316L regions in 10Fe (Fig. 4) with those in single component 316L (Fig. 3 (a)), very similar optical characteristics, with few visible interparticle boundaries, are observed. This implies a blend of 10 wt.% Fe powder in the mixture has not affected the interfacial bonding of the matrix 316L powder in 10Fe. By looking at the mixed 316L/Fe interfaces in 10Fe, cracks are observed, as shown in Fig. 4, perpendicular to the impact direction. These inter-lamellar cracks can be considered as indicators of either poor

interparticle bonding and/or a strong rebound of the impacted particles, which appears to explain the low DE of 10Fe (38%). It is also noticed that, the inter-lamellar cracks would mostly locate on the “top” of Fe and the “bottom” of 316L, as marked by red arrows. This observation implies a stronger rebound of 316L particles impacting on the previously deposited Fe compared with Fe on 316L.

3.2 Characterization of splats

3.2.1 Splat morphology

The desire to explain the feedstock deposition behavior, especially at the mixed interfaces, leads to the effort of performing splat tests onto coatings. The coating SEM morphologies after splat tests are shown in Fig. 5. Four types of impact scenarios are generated, referred to as 316L on 316L, 316L on Fe, Fe on 316L and Fe on Fe below.

Results show that the different splat impact scenarios between the 316L and Fe give significantly different splat morphologies. For 316L on Fe (Fig. 5 (b)), some splats have shown an obvious lifting off at the edges (circled in red). However, the opposite case Fe on 316L (Fig. 5 (c)), reveals splats all being closely attached to the coating surface. This finding correlates with the previous observation of the preferential location of inter-lamellar cracks at the 316L/Fe mixed interfaces (Fig. 4). As for the impacts between same material, i.e. 316L on 316L and Fe on Fe, it appears the 316L splats exhibit a closer contact to 316L surface than Fe to Fe, as the latter case also exhibits some splats with lifted edges (circled in red in Fig. 5 (d)). This phenomenon is also consistent with the poorer interfacial bonding of Fe/Fe than 316L/316L, as previously observed in Figs. 4 (a) and (b). Therefore, it is considered that the splat on coating tests can be indicative of the coating build-up process.

3.2.2 Splat deposition and deformation behavior

To quantify the splat deposition behavior, the bond ratio (BR) for each impact scenario is plotted in Fig. 6 (a). The BR results explicitly show the distinct deposition behavior of impacts between dissimilar materials, i.e. 316L on Fe and Fe on 316L (8% vs 87%); whereas the deposition behavior of impacts between the same material is relatively similar (316L on 316L-45%, Fe on Fe-38%).

To explain the splat deposition behavior, the deformation levels of the splat and the coating were both quantified. The splat deformation behavior shown in Fig. 6 (b) was evaluated using the common approach flattening ratio. The coating deformation shown in Fig. 6 (c) was evaluated by the average ratio of the depth of a crater over its diameter. It is believed this metric can normalize the effects of particle size and particle deforming on the coating deformation. Results show that the average FR values have a positive correlation with the BR results. The FR values can be explained by the relative particle/coating hardness, where a high FR is obtained from a soft particle impacting on the hard coating, e.g. Fe on 316L. Note that for the Fe splats with some irregular shape fractions, the splat FR might not reveal the actual particle deformation and is simply the splat aspect ratio. But it is believed that a high splat aspect ratio should similarly create a large particle/coating contact to facilitate deposition. As opposed to the splat deformation, in general, no correlations between the coating crater depth/diameter values and splat BR can be observed.

The rebound trend of a splat during impact was evaluated by the recoil coefficient e_r , which was determined from FE simulations (Section 2). The results for each impact scenario are plotted in Fig. 6 (d). In particular, a higher recoil coefficient is observed for the 316L on Fe (0.09)

than Fe on 316L (0.05), which implies a higher proportion of the splat kinetic energy is transformed to initiate the splat rebound upon impact for the former case. This explains the preferential location of inter-lamellar cracks in the 10Fe coating (Fig. 4) and also the lower BR of 316L on Fe than Fe on 316L (Fig. 6 (a)). However, the recoil coefficient metric is observed to fail to explain the different BR of a splat onto 316L and Fe coatings (e.g. 316L on 316L and 316L on Fe have the same e_r but different BR). This finding implies that, apart from rebound, there might be other factors affecting the splat deposition to occur, e.g. adhesion, which will be discussed in Section 3.2.3.

3.2.3 Splat adhesion strength/energy

To quantify and compare the relative splat bond strength between different impact scenarios, the splat adhesion testing was performed. The experimental approach used in this study was similar to the previous investigators Goldbaum et al. [24, 27], but the splats being measured were deposited onto as-polished cold sprayed coatings instead of the bulk material substrate. The typical load-displacement curve for each impact scenario and the respective SEM morphology of the failure region are shown in Fig. 7. Results show three main types of splat shearing behavior of the different impact scenarios between 316L and Fe can be observed.

The first type, which is seen in 316L on Fe, shows only a small rise in the tangential force with tip displacement, indicating a poor splat adhesion strength. The failure region exhibits a presence of crater with an approximate size of the original splat (contour circled in red). No visible shear tracks are observed in the crater. This indicates the splat adhesion was mainly through a weak conformal bonding.

The second type, which is illustrated by Fe on Fe and 316L on 316L, shows the failure regions revealing a crater, but its size is smaller than the original splat (contour circled in red). The difference in radius between the crater and original splat is roughly the width of the tangential force peak. The peripheral regions where the shearing events mainly took place implies the formation of metallurgical bond in these regions. Examination of the respective load-displacement curves, however, reveals some different situations. For Fe on Fe, the tangential force peak appears to be higher and wider than the 316L on Fe (first type), but the difference is not significant. However, for 316L on 316L, there was a sharp rise in the tangential force and then followed by a rapid drop, and the peak tangential force has reached a high value of about 360 mN.

Finally, the third type is the Fe on 316L. It can be seen the sheared region gives a full outline of the splat and the width of the tangential peak is roughly the width of the original splat (contour circled in red). This type of phenomenon is considered to be comparable to the behavior of shearing a bulk material, and thus the splat is expected to have a high adhesion strength approaching the theoretical shear strength of the materials at the counterpart. Compared with the previous case 316L on 316L (second type), the peak value of the tangential force is lower, but there is a much smoother rise and drop. This feature could indicate either a higher proportion of the metallurgical bond formation or degree of particle deformation during the Fe impact.

To further investigate the splat bonding features, the crater surfaces within the failure regions are shown in Fig. 8. For Fe on 316L (Fig. 8 (c)), a less well bonded splat (adhesion strength of 125 MPa) exhibiting the second type failure is presented instead. For 316L on 316L, some textures are observed at the crater surface. Considering that such features should not be resulted by the splat impact since the 316L powder has a smooth surface (Fig. 1), it is believed that they indicate the metallic bond formation at the crater region. For Fe on 316L and 316L on

Fe, similarly, textures can also be observed in the crater surfaces, but appear to be finer than those in 316L on 316L. For Fe on Fe, however, the crater surface appears to be relatively smooth, which implies the adhesion in the crater was simply the weak conformal bonding.

The adhesion strength and adhesion energy of each impact scenario were calculated from the respective load-displacement curve and are plotted in Fig. 9. As for the adhesion strength, the 316L on 316L (215 MPa) and Fe on 316L (167 MPa) are the two highest types, while the Fe on Fe and 316L on Fe types are the two lowest ones (<50 MPa). Regarding the adhesion energy, the Fe on 316L with a smooth shear curve (Fig. 7) exhibits the highest adhesion energy, even higher than 316L on 316L (3 vs 1.6 kJ/m²) despite its adhesion strength is lower (167 vs 215 MPa). Whereas the 316L on Fe and Fe on Fe types still exhibit a similar relative magnitude and remain the two lowest ones in adhesion energy. Moreover, it is noticed that the adhesion energy plots exhibit a positive correlation with the bond ratio results (Fig. 6 (a)). This results, combined with the rebound coefficient plots (Fig. 6 (d)), demonstrate the dominant contribution of adhesion energy in determining the splat BR.

4. Discussion

Previous results (Fig. 6 (a)) have shown the distinct splat deposition behavior between the four impact scenarios, especially for impacts between the dissimilar materials (316L on Fe and Fe on 316L), which corresponds to the mixed interface inter-lamellar cracks in the 10Fe coating (Fig. 4). To explain the splat deposition behavior, the powder characteristics (Table 1) and material properties (e.g. Table 3) of the feedstock were investigated. A few disparities between the 316L and Fe feedstocks are identified to be the contributing factors, i.e. hardness, surface oxide layer, and particle morphology, which are discussed individually as follows.

Hardness indicates the ability of a material to resist the plastic deformation. Generally in cold spray, the soft particle can exhibit a high degree of deformation (e.g. flattening) during impact, which enlarges the particle/substrate interface contact to facilitate the mechanical anchorage effect [24, 36]. The high level of deformation at the interfaces can also help to disrupt the surface oxide layer and provide a direct metal-metal contact favoring the metallic bond formation [36, 37]. In this study, the 316L powder has almost double the microhardness of the Fe (262.6 HV_{0.01} vs 141.3 HV_{0.01}). As the coatings on which splats deposit are the work hardened particle layers, most of the splat impact scenarios are categorized as the soft on hard case [30]. Thus, during cold spray, deformation at the impact interfaces tends to be mostly localized at the particle side rather than the coating. Comparing the impacts between dissimilar materials, the Fe on 316L type with a higher BR than 316L on Fe (87% vs 8%), corresponds to a higher particle FR (2.7 vs 2.2) and a shallower coating penetration (0.118 vs 0.144). Thus, it is considered for the soft on hard case, as the substrate is reluctant to deform during impact, the particle deformation can be more effective than the substrate deformation in facilitating particle deposition.

The splat deposition is considered as a competition between adhesion and rebound [35]. The hardness and the hardening behavior of the feedstock material also affect the rebound behavior of a splat during impact. According to Eq 5, a higher recoil coefficient (stronger rebound) is associated with a higher dynamic yield strength of a particle, which is determined by its static yield strength and the increment from effects of strain hardening, strain rate hardening and thermal softening during the kinetic impact process (Eq 3). As opposed to Fe, the 316L with a higher particle hardness implies a higher static yield strength, and its larger strain hardening parameter B and n (Table 2) also indicate a more rapid strain hardening behavior of the 316L during impact. Thus, this explains the stronger rebound of the 316L on Fe (preferentially located

inter-lamellar cracks at the 316L/Fe interfaces) and the lower BR (8% vs 87%), as compared with the Fe on 316L case.

During cold spray, the formation of adiabatic shear instabilities (e.g. metal jetting) at impact interfaces is an effective material behavior to remove the interfacial oxide layer, and the accompanying heat can induce a locally molten region to form strong metallurgical bond [36]. However, the jetting phenomenon of the deposited splats is not clearly observed in any of the four cases (Fig. 5). This observation implies that, under these cold spray conditions, there will be a significant interfacial oxide layer effect. The chromium content in 316L can form a thin but tenacious chromium surface oxide layer to protect the inner material from further oxidation [38, 39]; while the iron oxide is reported to be unstable/porous in nature [40] thus the oxide film tends to be thicker in Fe. The difference in the oxide film thickness between 316L and Fe can be indicated by the different interparticle boundary conditions shown in Fig. 3. Evidence of the effect of oxide layer interference was found at the crater surfaces within the sheared regions (Fig. 8), where the Fe/Fe crater surfaces are smoother than any interfaces involving the 316L. This implies that metallurgical bonding is inhibited in the Fe/Fe case, which could be due to the thicker oxide layer being harder to disrupt during impact. The difference in surface oxide film thickness between the 316L and Fe feedstocks can contribute to the ease of particle deposition (higher BR) on the 316L coating as opposed to the Fe coating (Fig. 6 (a)).

In the adhesion strength/energy plots (Fig. 9), comparing the Fe on 316L with 316L on 316L, it is noticed that the former case has a lower adhesion strength (167 vs 215 MPa) but its adhesion energy is almost double that of the latter (3 vs 1.6 kJ/m²). The high adhesion energy in Fe on 316L is attributed to its bulk-like shearing behavior during testing (Fig. 7), which implies the occurrence of either a higher proportion of metallurgical bond formation or degree of particle deformation during deposition. However, as discussed above, due to the thicker oxide film

presence in the Fe feedstock, theoretically the metallurgical bond formation in the Fe on 316L case should be less favored than in 316L on 316L. Also, the difference in splat deformation (splat FR: Fe on 316L-2.66 vs 316L on 316L-2.50) appears not significant enough to result in such different shearing behavior. Thus, it is believed there is a significant effect of the irregular splat morphology on the splat adhesion. As reported in literature, the large surface area provided by the irregular powder could increase the particle/substrate contact during deposition, thus the mechanical interlocking effect is enhanced (compared with spherical ones) [41]. Also, the irregular morphology increases the stress concentration at the particle surface during impact, which is expected to facilitate the localized shear deformation and disruption of the surface oxide layer to help the metallurgical bond formation [41]. However, the contribution of the irregular morphology on the splat adhesion has not yet been quantitatively determined.

Overall, this study presents an approach of performing splats tests onto as-polished coatings to investigate the mixed powder deposition behavior, which is often difficult to interpret from coating microstructure. Theoretically, this approach can be extended to investigate powder mixtures of any number of components. However, it is understood that there might be issues of using this approach. Firstly, the splat on coating tests have avoided the effects of roughness and tamping which will occur during the actual coating deposition. This simplification was justified in this case as the 316L and Fe feedstocks are similar in the particle size, velocity and density (Section 2). However, for other mixtures, e.g. hard/soft and large/small, where the tamping or retention effect of the component powder tends to be significant, the splat deposition behavior might not be indicative of the coating build-up process. Secondly, in order to investigate the 10Fe composite coating build-up process, the most straightforward approach is to directly spray single particles onto the as-polished 10Fe coatings. However, in this study an indirect approach was used as all splat tests were performed onto single component coatings for the ease of producing

the specific impact scenarios. This thus generates a concern of the effect of different substrates on the splat deposition. Relevant studies will be carried out in the future.

5. Conclusion

In this study, single component 316L, Fe, and a composite 10Fe coatings were cold spray deposited. A preferential location of inter-lamellar cracks was observed at the mixed 316L/Fe interfaces in the 10Fe coating. Splat tests were performed onto the as-polished single component 316L and Fe coatings and four types of impact scenarios (316L on 316L, 316L on Fe, Fe on 316L and Fe on Fe) were studied. Similar bonding features were observed in the deposited splats and cold sprayed coatings, showing the splat on coating tests to be indicative of the coating build-up process. To investigate the feedstock deposition behavior in the 10Fe coating, experimental characterizations (deformation, adhesion) and FE simulations (rebound behavior) of the splats were performed. Finally, the feedstock deposition behavior in the 10Fe coating was explained from hardness, surface oxide layer, and particle morphology.

Acknowledgements

The authors acknowledge the McGill Engineering Doctoral Awards (MEDA) and Natural Sciences and Engineering Research Council of Canada (NSERC) for the financial support. The authors are grateful for Prof. Jolanta Ewa Klemberg-Sapieha at Polytechnique Montréal for

access to the machine for splat adhesion tests. The authors thank Prof. Richard Chromik at McGill University for access to the optical profilometer.

References

- [1] C.-J. Li, G.-J. Yang, P.-H. Gao, J. Ma, Y.-Y. Wang, C.-X. Li, Characterization of nanostructured WC-Co deposited by cold spraying, *J. Therm. Spray Technol.* 16 (2007) 1011-1020.
- [2] H.-J. Kim, C.-H. Lee, S.-Y. Hwang, Fabrication of WC-Co coatings by cold spray deposition, *Surf. Coat. Technol.* 191 (2005) 335-340.
- [3] N. Melendez, A. McDonald, Development of WC-based metal matrix composite coatings using low-pressure cold gas dynamic spraying, *Surf. Coat. Technol.* 214 (2013) 101-109.
- [4] P.-H. Gao, C.-J. Li, G.-J. Yang, Y.-G. Li, C.-X. Li, Influence of substrate hardness transition on built-up of nanostructured WC-12Co by cold spraying, *Appl. Surf. Sci.* 256 (2010) 2263-2268.
- [5] P.-H. Gao, Y.-G. Li, C.-J. Li, G.-J. Yang, C.-X. Li, Influence of powder porous structure on the deposition behavior of cold-sprayed WC-12Co coatings, *J. Therm. Spray Technol.* 17 (2008) 742-749.
- [6] R. Lima, J. Karthikeyan, C. Kay, J. Lindemann, C. Berndt, Microstructural characteristics of cold-sprayed nanostructured WC-Co coatings, *Thin solid films* 416 (2002) 129-135.
- [7] K.J. Hodder, J.A. Nychka, A.G. McDonald, Comparison of 10 μm and 20 nm Al-Al₂O₃ Metal Matrix Composite Coatings Fabricated by Low-Pressure Cold Gas Dynamic Spraying, *J. Therm. Spray Technol.* 23 (2014) 839-848.
- [8] H. Koivuluoto, P. Vuoristo, Effect of Powder Type and Composition on Structure and Mechanical Properties of Cu + Al₂O₃ Coatings Prepared by using Low-Pressure Cold Spray Process, *J. Therm. Spray Technol.* 19 (2010) 1081-1092.
- [9] K. Spencer, D.M. Fabijanic, M.X. Zhang, The influence of Al₂O₃ reinforcement on the properties of stainless steel cold spray coatings, *Surf. Coat. Technol.* 206 (2012) 3275-3282.
- [10] H.Y. Lee, S.H. Jung, S.Y. Lee, Y.H. You, K.H. Ko, Correlation between Al₂O₃ particles and interface of Al-Al₂O₃ coatings by cold spray, *Appl. Surf. Sci.* 252 (2005) 1891-1898.
- [11] Y. Tao, T. Xiong, C. Sun, H. Jin, H. Du, T. Li, Effect of α -Al₂O₃ on the properties of cold sprayed Al/ α -Al₂O₃ composite coatings on AZ91D magnesium alloy, *Appl. Surf. Sci.* 256 (2009) 261-266.

- [12] X.-k. Wu, X.-l. Zhou, H. Cui, X. Zheng, J.-s. Zhang, Deposition Behavior and Characteristics of Cold-Sprayed Cu-Cr Composite Deposits, *J. Therm. Spray Technol.* 21 (2012) 792-799.
- [13] H. Che, X. Chu, P. Vo, S. Yue, Cold spray of mixed metal powders on carbon fibre reinforced polymers, *Surf. Coat. Technol.* 329 (2017) 232-243.
- [14] A. Sova, R. Maestracci, M. Jeandin, P. Bertrand, I. Smurov, Kinetics of composite coating formation process in cold spray: Modelling and experimental validation, *Surf. Coat. Technol.* 318 (2017) 309-314.
- [15] A. Moridi, S.M. Hassani-Gangaraj, M. Guagliano, M. Dao, Cold spray coating: review of material systems and future perspectives, *Surf. Eng.* 30 (2014) 369-395.
- [16] S. Grigoriev, A. Okunkova, A. Sova, P. Bertrand, I. Smurov, Cold spraying: From process fundamentals towards advanced applications, *Surf. Coat. Technol.* 268 (2015) 77-84.
- [17] X.-T. Luo, Y.-K. Wei, Y. Wang, C.-J. Li, Microstructure and mechanical property of Ti and Ti6Al4V prepared by an in-situ shot peening assisted cold spraying, *Materials & Design* 85 (2015) 527-533.
- [18] R.G. Maev, V. Leshchynsky, Air gas dynamic spraying of powder mixtures: theory and application, *J. Therm. Spray Technol.* 15 (2006) 198-205.
- [19] H. Koivuluoto, P. Vuoristo, Effect of Ceramic Particles on Properties of Cold-Sprayed Ni-20Cr+Al₂O₃ Coatings, *J. Therm. Spray Technol.* 18 (2009) 555-562.
- [20] E. Irissou, J.-G. Legoux, B. Arsenault, C. Moreau, Investigation of Al-Al₂O₃ cold spray coating formation and properties, *J. Therm. Spray Technol.* 16 (2007) 661-668.
- [21] H. Aydin, M. Alomair, W. Wong, P. Vo, S. Yue, Cold Sprayability of Mixed Commercial Purity Ti Plus Ti6Al4V Metal Powders, *J. Therm. Spray Technol.* 26 (2017) 1-11.
- [22] T. Van Steenkiste, J. Smith, R. Teets, Aluminum coatings via kinetic spray with relatively large powder particles, *Surf. Coat. Technol.* 154 (2002) 237-252.
- [23] Y. Xiong, G. Bae, X. Xiong, C. Lee, The Effects of Successive Impacts and Cold Welds on the Deposition Onset of Cold Spray Coatings, *J. Therm. Spray Technol.* 19 (2009) 575-585.
- [24] D. Goldbaum, J.M. Shockley, R.R. Chromik, A. Rezaeian, S. Yue, J.-G. Legoux, E. Irissou, The Effect of Deposition Conditions on Adhesion Strength of Ti and Ti6Al4V Cold Spray Splats, *J. Therm. Spray Technol.* 21 (2011) 288-303.
- [25] F. Meng, S. Yue, J. Song, Quantitative prediction of critical velocity and deposition efficiency in cold-spray: A finite-element study, *Scr. Mater.* 107 (2015) 83-87.

- [26] X. Chu, H. Che, P. Vo, R. Chakrabarty, B. Sun, J. Song, S. Yue, Understanding the cold spray deposition efficiencies of 316L/Fe mixed powders by performing splat tests onto as-polished coatings, *Surf. Coat. Technol.* 324 (2017) 353-360.
- [27] R.R. Chromik, D. Goldbaum, J.M. Shockley, S. Yue, E. Irissou, J.-G. Legoux, N.X. Randall, Modified ball bond shear test for determination of adhesion strength of cold spray splats, *Surf. Coat. Technol.* 205 (2010) 1409-1414.
- [28] D. Simulia, Abaqus 6.11 analysis user's manual, Abaqus 6.11 Documentation (2011) 22.22.
- [29] H. Assadi, F. Gärtner, T. Stoltenhoff, H. Kreye, Bonding mechanism in cold gas spraying, *Acta Materialia* 51 (2003) 4379-4394.
- [30] G. Bae, Y. Xiong, S. Kumar, K. Kang, C. Lee, General aspects of interface bonding in kinetic sprayed coatings, *Acta Materialia* 56 (2008) 4858-4868.
- [31] G.R. Johnson, W.H. Cook, A constitutive model and data for metals subjected to large strains, high strain rates and high temperatures, *Proceedings of the 7th International Symposium on Ballistics*, The Hague, The Netherlands, 1983, pp. 541-547.
- [32] M. Grujicic, C.L. Zhao, W.S. DeRosset, D. Helfrich, Adiabatic shear instability based mechanism for particles/substrate bonding in the cold-gas dynamic-spray process, *Materials & Design* 25 (2004) 681-688.
- [33] A.A. Olleak, M.N. Nasr, H.A. El-Hofy, The Influence of Johnson-Cook Parameters on SPH Modeling of Orthogonal Cutting of AISI 316L, (2015).
- [34] O. Bielousova, J. Kocimski, R.G. Maev, I. Smurov, W. Scharff, V. Leshchynsky, Localisation of deformation in cold gas dynamic spraying, *Surf. Eng.* 32 (2016) 655-662.
- [35] J. Wu, H. Fang, S. Yoon, H. Kim, C. Lee, The rebound phenomenon in kinetic spraying deposition, *Scr. Mater.* 54 (2006) 665-669.
- [36] T. Hussain, D.G. McCartney, P.H. Shipway, D. Zhang, Bonding Mechanisms in Cold Spraying: The Contributions of Metallurgical and Mechanical Components, *J. Therm. Spray Technol.* 18 (2009) 364-379.
- [37] T. Samson, D. MacDonald, R. Fernández, B. Jodoin, Effect of Pulsed Waterjet Surface Preparation on the Adhesion Strength of Cold Gas Dynamic Sprayed Aluminum Coatings, *J. Therm. Spray Technol.* 24 (2015) 984-993.
- [38] P.S. Korinko, S.H. Malene, Considerations for the weldability of types 304L and 316L stainless steel, *Practical Failure Analysis* 1 (2001) 61-68.
- [39] S. Tardio, M.-L. Abel, R.H. Carr, J.E. Castle, J.F. Watts, Comparative study of the native oxide on 316L stainless steel by XPS and ToF-SIMS, *Journal of Vacuum Science & Technology A: Vacuum, Surfaces, and Films* 33 (2015) 05E122.

[40] C. Leygraf, I.O. Wallinder, J. Tidblad, T. Graedel, Atmospheric Corrosion, Wiley, 2016.

[41] L. Ajdelsztajn, B. Jodoin, J.M. Schoenung, Synthesis and mechanical properties of nanocrystalline Ni coatings produced by cold gas dynamic spraying, Surf. Coat. Technol. 201 (2006) 1166-1172.

Table 1 Characteristics of the feedstock powder.

Powder	Morphology	Size, μm	Microhardness, $\text{HV}_{0.01}$
316L	Spherical	22.2	262.6
Fe	Spherical, irregular	29.1	141.3

Table 2 Process details for coating deposition and splat tests.

Type	Feedstock	Substrate	Gun speed, mm/s	Feed rate, g/min	
				316L	Fe
Coating deposition	316L			23.8	-
	10Fe	Mild steel	300	18.3	2.4
	Fe			-	21.7
Splat test	316L	316L and Fe	1000	8.5	-
	Fe	coatings		-	11

Table 3 Material properties and parameters for the Johnson-Cook model [33, 34].

Properties	Parameter	Unit	Value	
			316L	Fe
<i>General</i>	Density	kg/m ³	8000	7890
	Specific heat	J/kg · K	500	452
	T_m	K	1668	1811
<i>Elastic</i>	Young's modulus	GPa	193	207
	Poison's ratio	–	0.27	0.29
<i>Plastic</i>	A	MPa	514	175
	B	MPa	514	380
	n	–	0.508	0.32
	C	–	0.042	0.06
	m	–	0.533	0.55
	T_{ref}	K	293	293

Figure captions

Fig. 1 SEM images of the feedstock powders.

Fig. 2 Optical images of a splat before (top left) and after shearing (bottom left), and the respective load-displacement curve.

Fig. 3 SEM/EDS analyses on 316L (DE-55%) and Fe (DE-50%): (a) BSE image of 316L, (b) EDS spectrum of 316L, (c) BSE image of Fe, and (d) EDS spectrum of Fe.

Fig. 4 BSE image of 10Fe (DE-38%). Red arrows: inter-lamellar cracks at the mixed 316L/Fe interfaces.

Fig. 5 SEM coating morphology after splat tests: (a) 316L on 316L, (b) 316L on Fe, (c) Fe on 316L, and (d) Fe on Fe.

Fig. 6 The (a) bond ratio, (b) splat flattening ratio, (c) coating crater depth/size, and (d) recoil coefficient (from FE simulations) for each impact scenario.

Fig. 7 Typical tangential force vs displacement curve with the respective SEM image of the failure region for each impact scenario (Red circles: contours of the original splats).

Fig. 8 High magnification SEM morphology of the crater failure surface: (a) 316L on 316L, (b) 316L on Fe, (c) Fe on 316L, and (d) Fe on Fe.

Fig. 9 Splat adhesion strength and adhesion energy for each impact scenario.

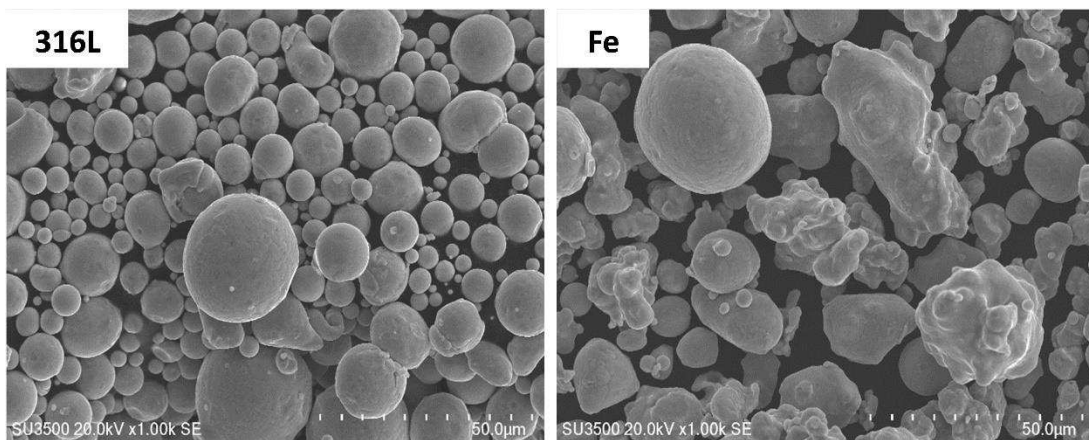


Fig. 1

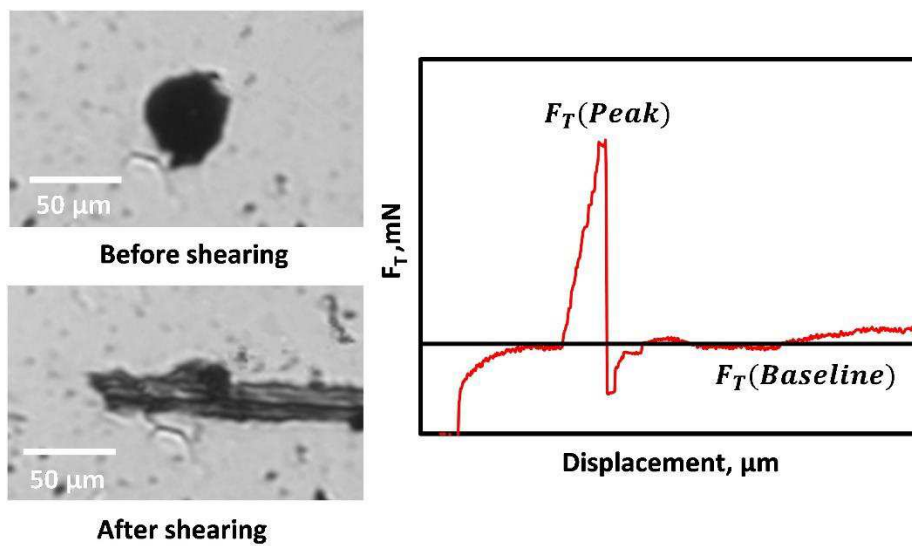


Fig. 2

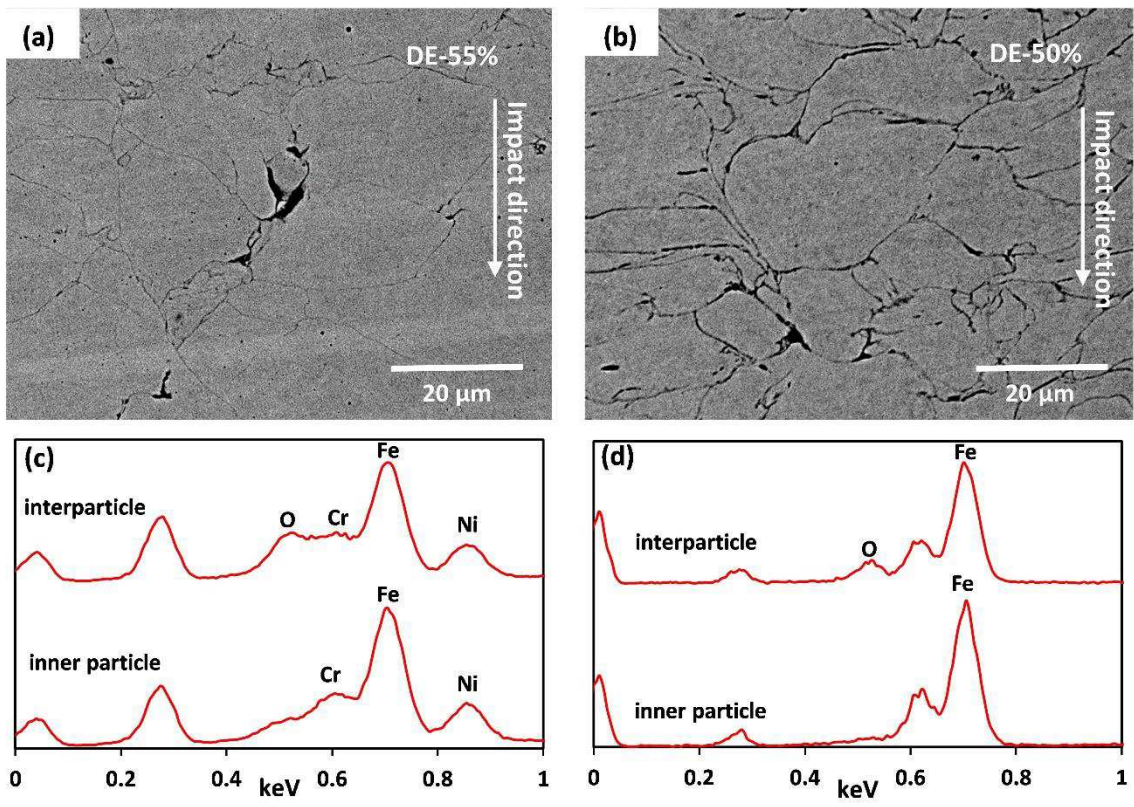


Fig. 3

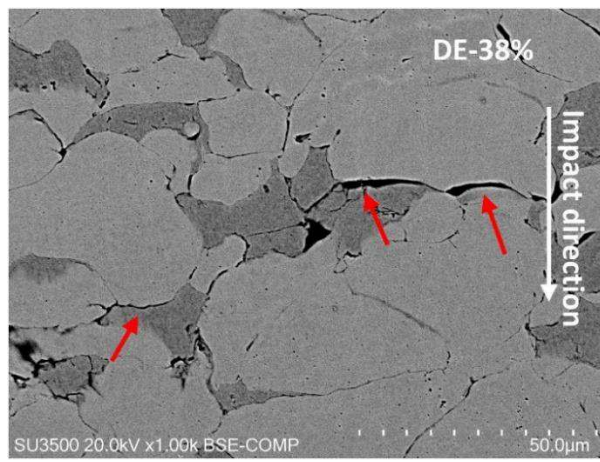


Fig. 4

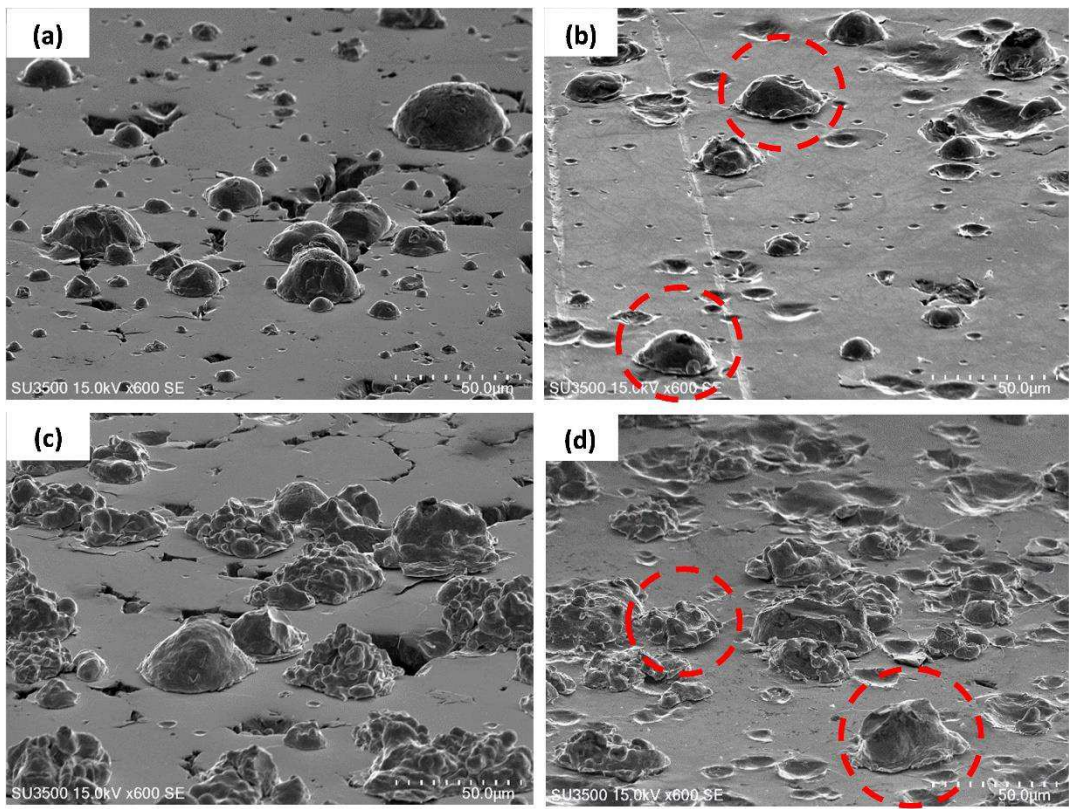


Fig. 5

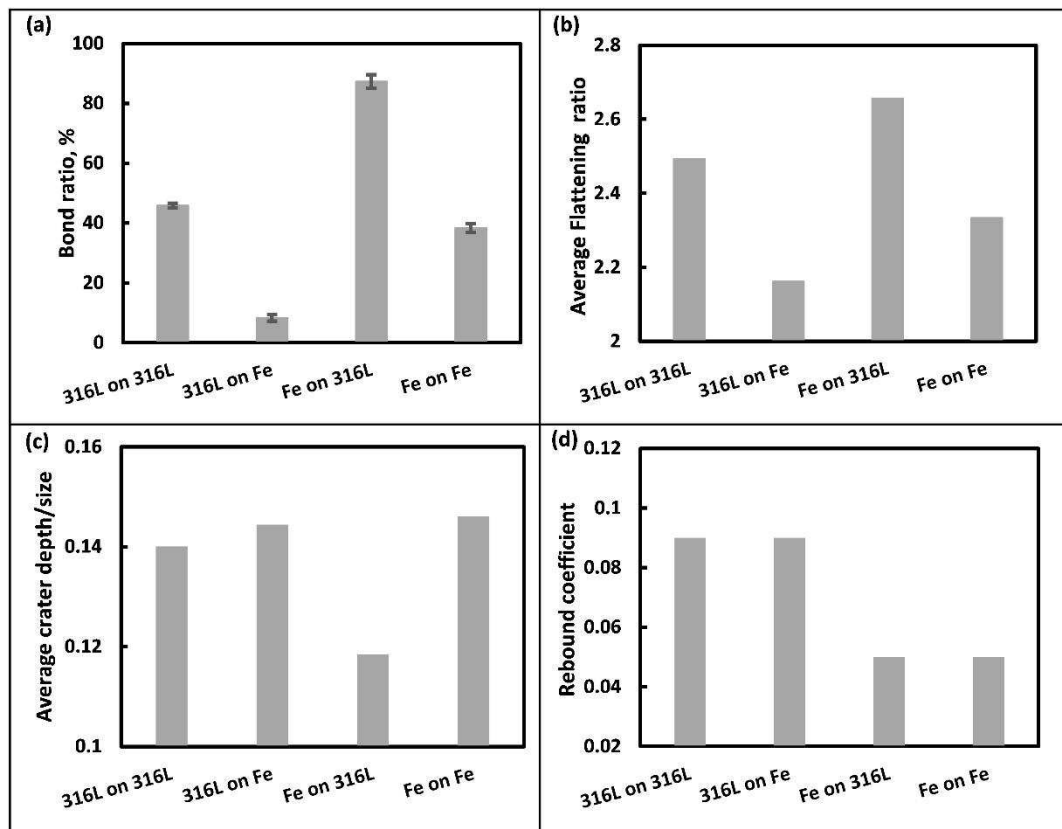


Fig. 6

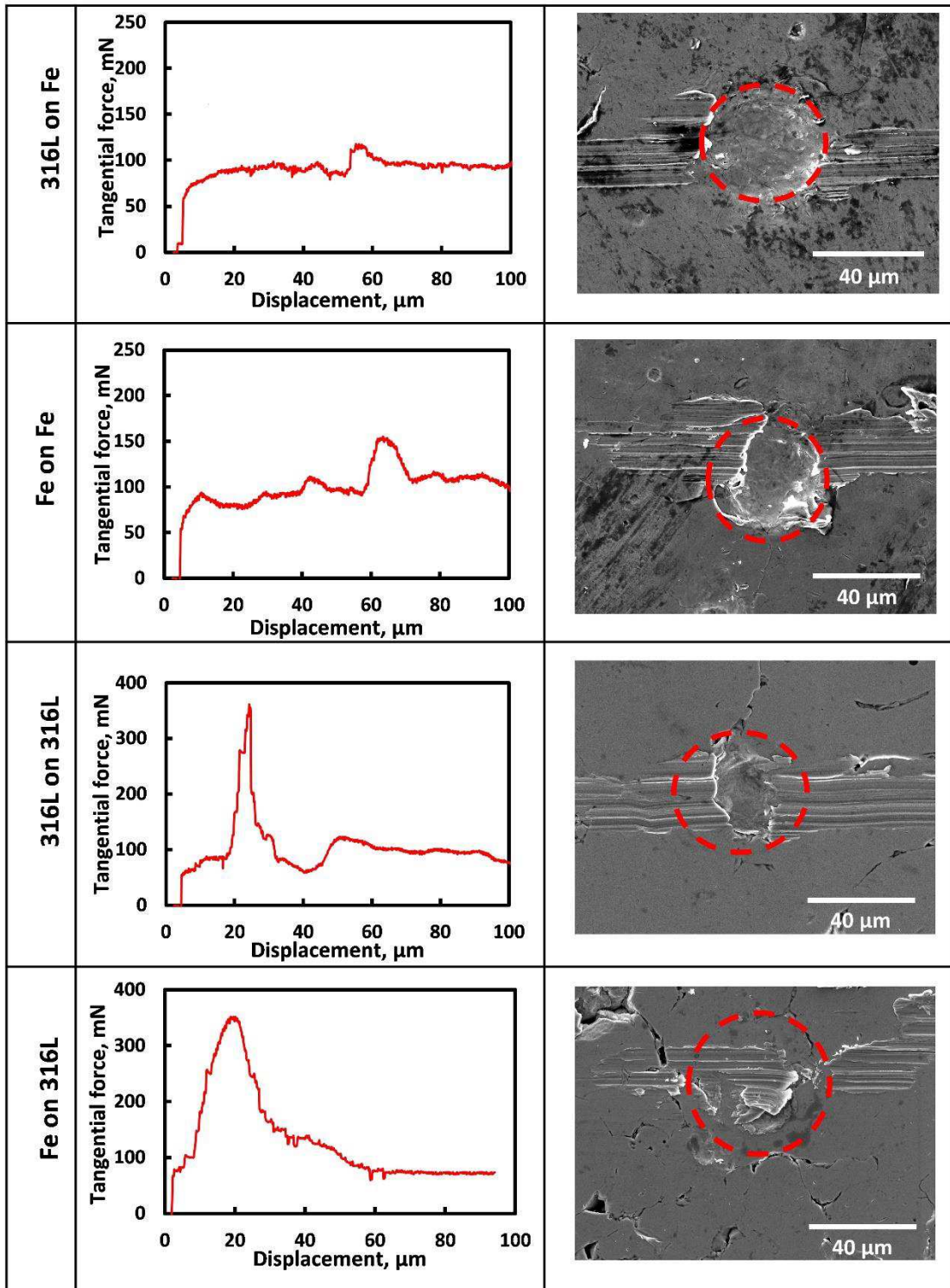


Fig. 7

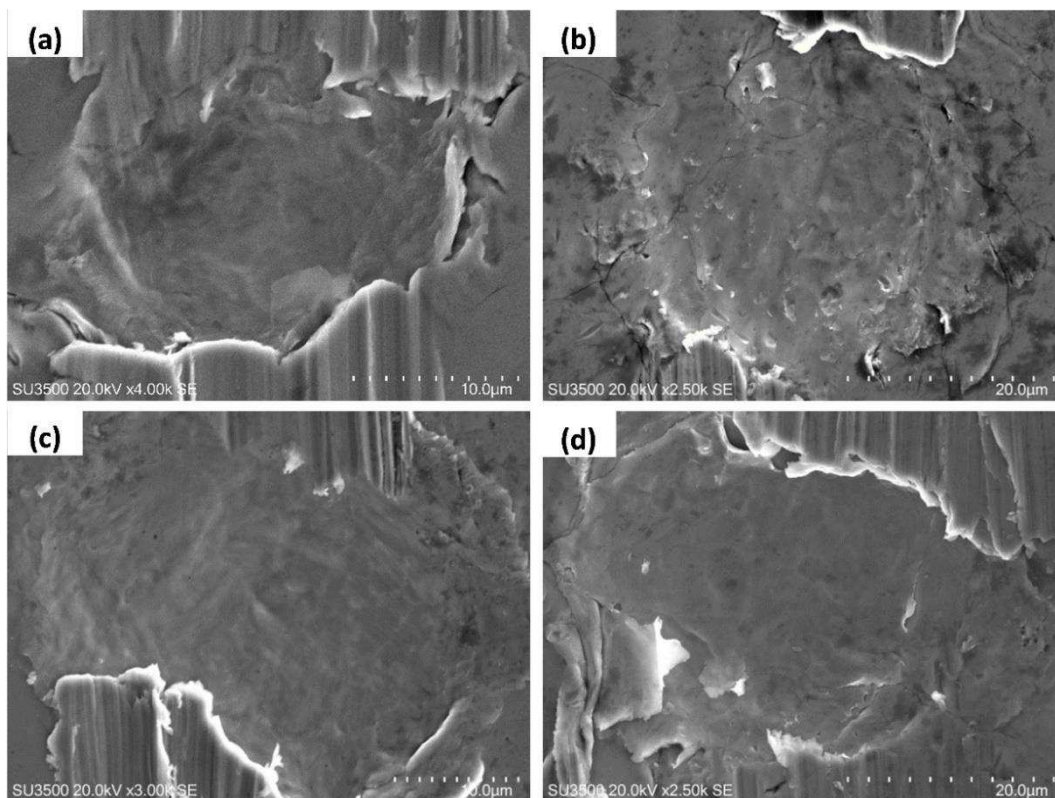


Fig. 8

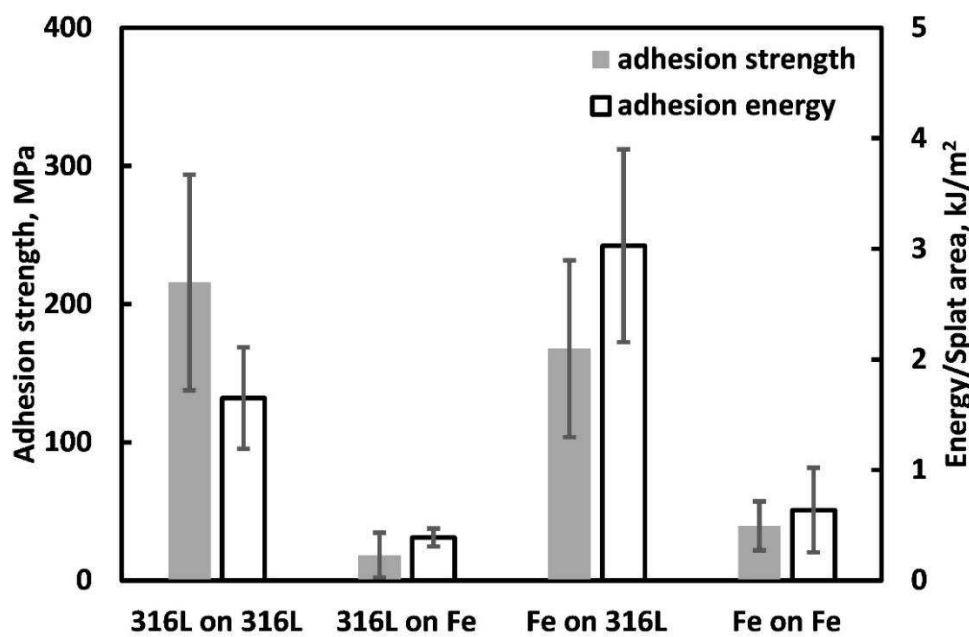


Fig. 9